

Development of cryogenic X-ray detectors based on Mo/Au Transition Edge Sensors

C. Pobes, L. Fàbrega, A. Camón, N. Casañ-Pastor, P. Strichovanec, J. Sesé, J. Moral-Vico, R. Jáudenes

Abstract—We report on the development of Mo/Au based Transition Edge Sensors (TESs) aimed at soft X-ray detection. TESs of different sizes with $T_c \sim 100$ mK and very narrow transitions have been fabricated. Dark characterization based on I-V, complex impedance and noise measurements has allowed us to obtain their basic functional parameters at different bath temperatures and operating points. Electrodeposited Bi films, to be used as X-ray absorbers, have been developed and characterized.

Index Terms—Transition Edge Sensors, X-ray spectroscopy, proximity effect, radiation detectors

I. INTRODUCTION

THIN proximity bilayers, combining a superconductor layer and a normal metal layer in close contact, are the basic constituent of TESs [1]. TESs are very sensitive thermometers when operating at their superconducting transition temperature (T_c), which can be easily tuned between 100 mK and 400 mK. When coupled to a suitable absorber, TESs become radiation detectors with outstanding spectroscopic capabilities; this makes them extremely interesting for a variety of instruments which require high sensitivity and resolution. TES detectors are already in use in a wide range of applications, including astronomy, nanotechnology, biomedicine, security and industry, and are being projected as essential elements in very demanding future experiments and space missions such as the X-IFU instrument in ESA's X-ray telescope ATHENA [2].

TES parameters are very sensitive to the used materials, to the design, and to the fabrication process, and they need to be optimized for each application. Mo [3], [4] and Ti [5] based TESs with $T_c \sim 100$ mK have demonstrated excellent performances for X-ray detectors [6], [2]. The choice of absorber material is also specific to the radiation to be

detected. For X-rays, layers several micrometers thick of a material with high stopping power and suitable heat capacity, thermal conductivity and electrical conductivity are required; Bi and Au/Bi layers are most convenient [7], [2].

We report on the fabrication and dark characterization of Mo/Au-based TESs for X-ray detection. Earlier reported designs and fabrication processes [8]-[11] have been upgraded, with the result of improved reproducibility and quality of the devices. Dark characterization of bare sensors with different parameters has been performed; IV curves, $Z(\omega)$ and noise measurements are used to extract fundamental parameters of the TESs and explore their dependences on the bath temperature and the operating point. In parallel, we report on the optimization of electrodeposited Bi films to be integrated in the devices as X-ray absorbers.

II. FABRICATION PROCESS

A. TES fabrication

TESs are fabricated on low stress Si_3N_4 membranes of 0.5 μm and 1 μm thicknesses. Square membranes of lateral size 0.5 mm and 1 mm are fabricated from wafers provided by Si-Mat by Reactive Ion Etching (RIE).

Mo/Au bilayers are deposited at room temperature using the trilayer design [10]. First, Mo is deposited by RF magnetron sputtering in a UHV chamber (base pressure $< 10^{-7}$ mbar); standard conditions are 280 W and 0.3 mbar Ar pressure. Next, a 15 nm Au layer is deposited in situ by DC magnetron sputtering in order to prevent oxidation of the Mo surface and thus degradation of the Mo/Au interface. Finally, the desired thickness of Au is completed by electron beam deposition in another chamber. Typical residual resistivity values of Mo, sputtered Au, and e-beam Au layers are respectively 116, 38 and 3.96 $\text{n}\Omega\text{m}$ in the thickness ranges of interest.

In order to achieve a T_c near 100 mK, which is a design goal for X-ray detection, Mo thickness was fixed at 55 nm, well above the range displaying 2-D effects [12], and the Au thickness was increased up to the required value, which turned out to be 340 nm (15 nm by sputtering, 325 nm by e-beam). This leads to sensors with an R_n on the order of 10 $\text{m}\Omega$. The Mo thickness can be reduced and thus also the Au needed to achieve 100 mK, leading to sensors with higher R_n . After deposition, the bilayer squares are defined to the desired size (between 100 μm and 200 μm in this work) by optical photolithography using a positive photoresist mask. Later, Au banks are added to ensure sharp transitions in the devices [13]. Finally, Nb pads and wiring are fabricated by DC sputtering and a lift-off process. The optimization of the fabrication

Manuscript received September 5, 2016. Work financed by the Spanish Ministerio de Economía y Competitividad-MINECO (projects ESP2014-53672-C3-2-P and ESP2014-59309-JIN), the European Space Agency-ESA (CTP Contract "Optimization of a European TES array") and the European Commission (H2020 project AHEAD: "Integrated activities for the high energy astrophysics domain"). Personnel from ICMAB acknowledge financial support from MINECO, through the "Severo Ochoa" Program for Centers of Excellence in R&D (SEV- 2015-0496). RMJ wishes to thank MINECO for her FPI contract. We thank PTB for providing the SQUIDS.

C. P., A. C., R. J. and P. S. authors are with the Instituto de Ciencia de Materiales de Aragón (ICMA) and Departamento de Física de la Materia Condensada. CSIC-Universidad de Zaragoza. Zaragoza 50009, Spain (e-mail:cpobes@unizar.es)

L. F., N. C., J. M. and R. J. authors are with the ICMAB-CSIC, Campus de la UAB, E-08193 Bellaterra, Spain

J. S. author is with the Instituto de Nanociencia de Aragón (INA) Universidad de Zaragoza. Zaragoza 50018, Spain

process lead to very sharp (<5 mK) and reproducible transitions.

B. Bi electrodeposition

Electrodeposition of Bi films on gold plated (Au thickness 10 nm) glass and wafers has been developed, for thicknesses in the range of interest (4-6 μm). Several electrodeposition strategies and electrolyte solutions were tested to tune morphology and uniformity, in order to obtain films with compactness and electrical and thermal conduction suitable to be used as X-ray absorbers.

All Bi films are polycrystalline and are formed by very high quality rhombohedral crystals, as determined from X-ray diffraction patterns. X-ray Photoelectron Spectroscopy (XPS) spectra of Bi (4f peaks) show the presence of pure, metallic Bi, except in a very narrow surface layer (~10-20 nm) where Bi is oxidized (Fig. 1b). Crystal sizes depend on the electrolyte and deposition conditions used. Optimal deposits are favoured by electrodynamic deposition and by heating.

A clear correlation between morphology (compactness and grain size) and electrical resistance is observed [14]. Two different routes have produced so far the best coatings: one with a simpler electrolyte (solution 1), containing 10 M Bi(NO₃)₃·5H₂O (Aldrich, 99.999%) and 1 M HNO₃ (Sigma-Aldrich, 70%) [15], [16], and another with a more complex electrolyte (solution 2), containing 0.15 M Bi(NO₃)₃·5H₂O (Aldrich, 99.999%), 1.35 M glycerol (Sigma-Aldrich, ≥99.5%), 0.33 M DL-tartaric acid (Aldrich, 99%), 1.15 M KOH (Sigma-Aldrich, ≥85%) and HNO₃ added up to a pH of 0 [17].

Fig. 1 (left) displays Scanning Electron Microscope images of the microstructure and profile of a 6 μm thick film obtained under optimal conditions. Fig. 2 displays the resistivity of two optimal films, obtained with the conditions found optimal for solutions 1 and 2, as compared with an example far from optimal. Thin Bi films usually display semiconductor behaviour [18] rather than the semimetal character of bulk Bi. Therefore, optimal films should have residual resistance ratios $R_{RR} = \rho(300\text{ K})/\rho(2\text{ K})$ as close to unity as possible, and room temperature resistivity as close to the bulk value (0.13 mΩcm) as possible. Our best films display $R_{RR} \sim 0.84-0.9$ and $\rho(300\text{ K}) \sim 0.2-0.3\text{ m}\Omega\text{cm}$. These values are close to the best ones reported to date for other Bi electrodeposited films of similar thickness [7] and evidence that the addition of an Au layer to the absorber might be required to improve its thermal conductance.

FIG.1 HERE

FIG.2 HERE

III. CHARACTERIZATION SET-UP

TESs have been characterized in a dedicated holder of a dilution refrigerator coupled to a SQUID, generation C6, type X216, with a nominal current noise of 3 pA/Hz^{0.5} provided by PTB [19]. The bias circuit uses a parallel shunt resistance,

TABLE I

BASIC PARAMETERS OF TES CHARACTERIZED

	Device_A	Device_B	Device_C
Size(μm)	200x200	150x150	100x100
Membrane(mm)	1x1	0.5x0.5	0.5x0.5
T _c (mK)	115	91	90
R _n (mΩ)	14.9	12.5	8.9
G(pW/K)	300-320	130-140	75-95
n	3.1-3.3	3.1-3.3	3.0-3.2

Basic parameters of the three bare TESs with T_c near 100 mK characterized in this work. In all of them the Mo/Au bilayers are 55nm/340nm and the membrane thickness is 500 nm. Listed device sizes are Mo/Au areas. The ranges cover the spread as %R_n is varied.

R_{sh} = 2 mΩ, small compared with the R_n of the TES, which results in an effective voltage bias for most of the transition and thus a stabilizing negative electrothermal feedback [1].

A. IV measurements

IV curves have been recorded at various bath temperatures T_{bath} from 30 mK (slightly over the lowest achieved with our refrigerator) to the T_c of the TESs. The TES is driven into normal state by a current I_{bias} above the critical current value. Then I_{bias} is reduced and the output voltage V_{out} is recorded. The experimental I_{bias}-V_{out} values are converted into TES related values, I_{TES}-V_{TES}. From the slopes of the curves in normal and superconducting states the parasitic resistance of the circuit (R_{par}) and the normal state resistance R_n of the TES are deduced.

Finally, from the curves of power P_{TES} versus resistance R_{TES} in the TES, a value of P_{TES} at every T_{bath} is extracted. This can be done at various possible operating points of the TES, identified as %R_n. Usually a high %R_n is selected [20],[21] The P_{TES}-T_{bath} curve is fitted to a power law, which allows to estimate the conductance G of the TES to the thermal bath by means of:

$$P_{TES} = K(T_c^n - T^n) \quad (1a)$$

$$G = nKT_c^{(n-1)} \quad (1b)$$

where K is a geometry dependent factor, and the exponent n, which usually takes values between 3 and 4, depends on the dominant heat conduction mechanism [1]. In the fit, T_c can be allowed to vary and compared with direct estimates from R(T) measurements.

B. Complex Impedance measurements

Complex impedance measurements are used to study the dynamic behavior of the TES and, through fits to a suitable thermal model, to extract the fundamental functional parameters of the devices. The logarithmic sensitivities to temperature (α_i) and current (β_i), and the effective time constant τ_{eff} can be determined at different operating points and bath temperatures. The heat capacity C of the TES can also be deduced from these data with the use of the G extracted from the IV measurements [22]-[25].

$Z(\omega)$ measurements were performed by carrying out frequency sweeps at different bath temperatures and operating

TABLE II
FUNCTIONAL PARAMETERS FROM DARK CHARACTERIZATION

	Device_A	Device_B	Device_C
$C(\text{fJ/K})$	300-370	65-85	30-50
$\tau_{\text{eff}}(\mu\text{s})$	50-400	40-140	40-160
L_0	3-21	5-15	2-9
$R_0(\text{m}\Omega)$	7.4	6.2	4.5
$P_0(\text{pW})$	4.9	0.5-3.5	0-2.4
α_1	90-150	50-75	40-85
β_1	0.12-0.20	0.25-0.35	0.18-0.35

Parameters of three TESs with T_c near 100 mK at 50% of R_n , R_o and P_o are respectively the resistance and power at this operating point while L_0 is the loop gain. The ranges cover the spread as T_{bath} is varied.

points along the superconducting transition. From the experimental transfer functions measured in the superconducting (TFS) and normal (TFN) states, an independent estimate of R_n can be made and the inductance L of the circuit can be obtained. The TES impedance Z_{TES} at every operating point is then deduced from the measured TF at that point and the TFS .

For our measurements a HP3562A spectrum analyzer is used. The equipment can be configured in sine sweep mode and the frequency is varied from 10 Hz up to 100 KHz. The TF can be displayed selecting Nyquist mode and then read with a PC. Z_{TES} is calculated as:

$$Z_{\text{TES}} = \left(\frac{TFS}{TF} - 1\right) (R_{sh} + R_{par} + i\omega L) \quad (2)$$

The process has been automatized to scan the superconducting transition at different points for every T_{bath} .

C. Noise Measurements

The HP3562A can also be configured to acquire noise spectra. The same acquisition program used for complex impedance measurements is instructed to take noise spectra at each point. The measured noise in $\text{V/Hz}^{0.5}$ is then converted into TES noise in $\text{pA/Hz}^{0.5}$ and compared with TES noise models [1],[20].

IV. RESULTS

Three devices (bare TESs without absorber) have been characterized in this work. Their basic and main functional parameters are listed in Tables I and II.

R_n values summarized in Table I depend on the device size because this refers to the Mo/Au bilayer after etching. When taking into account the Nb pads and Au banks, the reported R_n values scale with the effective area of the devices and are compatible with a single square resistance value.

Conductance parameters (n , K , G) are obtained from I-V curves measured at different T_{bath} temperatures ranging from 30 mK up to the critical temperature of the devices and fitting the data to (1).

Fig. 3 shows typical Z_{TES} curves at a fixed T_{bath} and for different operating points along the superconducting transition. Fits to a single thermal block model (SBM) are also displayed. The SBM assumes a single heat capacity C (the TES capacity) coupled to the bath through a single conductance G (provided by the membrane). As can be seen, this simple model is not enough to reproduce the detailed TES behavior, even in these sensors without absorber. More complex models with additional thermal blocks are required, as reported in other works [26]-[31]. The simplest extension (two thermal blocks) assumes an extra C coming either from the membrane or from the decoupling of the electrons and phonons in the TES; both cases may result in quite similar $Z(\omega)$, also nearly indistinguishable from the SBM fits [28]. Three block models will be considered to better reproduce the experimental data. Nevertheless, we use fits to the single-block model [22]-[25] to get preliminary estimates of the main TES parameters, τ_{eff} , α_1 , β_1 , C , and the low frequency loop gain $L_0 = P_0\alpha_1/GT_0$. Results at a fixed operating point (50% R_n) are shown in Table II; the value ranges displayed for each parameter correspond to the parameter spread as T_{bath} is varied. Our devices display α_1 values between 40 and 150; a monotonous decrease of this parameter as % R_n increases is observed for all the measured TES; the behavior as a function of T_{bath} is less clear, but it appears that α_1 is rather constant and increases only very close to T_c .

The C values of device_B and device_C scale with area, while device_A displays a value nearly twice as high than expected; it must be taken into account that superconductors display a discontinuity of C at the transition, and thus the measured values may not be proportional to size. However, another possible explanation for the larger C of device_A is a contribution of the membrane, which might act as an additional thermal block, as argued above. Further measurements are planned to understand this behavior.

Fig. 4 (bottom) shows the β_1 parameter for the three TESs measured versus R_{TES} . As it might be expected from the TESs sizes, they fall in the range ascribed to the Phase Slipping Line regime according to the analysis performed by Bennett and Ullom in [6].

FIG.3 HERE

FIG.4 HERE

Lastly, Fig. 5 displays noise spectra recorded for one of the devices and the estimates using a SBM; these calculations include three components: the thermal fluctuation noise (between the single block and the bath), the Johnson noise in the TES and the Johnson noise in the shunt resistance. An additional constant $3 \text{ pA/Hz}^{0.5}$ contribution is added in quadrature to account for the noise from the SQUID. Comparison of measured data with SBM estimates shows that noise is well reproduced when the TES works near its normal state but an excess noise appears in the middle of the transition being higher at lower T_{bath} and frequencies. This behavior points to a thermal nature of this excess noise. A possible origin is the lack of proper EMI shielding in the device. Further studies are planned to assess this effect.

FIG.5 HERE

V. CONCLUSIONS

Mo/Au based TESs with T_c near 100 mK and values of R_n around 10 m Ω have been fabricated. Full dark characterization of several devices has allowed preliminary estimates of their basic parameters as a function of bath temperature and operating point. We observed that even for these bare devices, the behavior cannot be reproduced by a single thermal block model. Electrodeposited Bi films have been developed to be integrated as X-ray absorbers into a full detector.

REFERENCES

- [1] K. D. Irwin and C.C. Hilton, "Transition-Edge Sensors in Cryogenic Particle Detection", edited by C. Enss, Springer-Verlag, Berlin Heidelberg, *Topics in Applied Physics*, vol. 99 pp. 63–149, 2005.
- [2] S.J. Smith et al., "Transition-edge sensor pixel parameter design of the microcalorimeter array for the X-ray Integral Field Unit on Athena", *Proceed. SPIE Conf. Series*, vol 9905, 9905H, 2016.
- [3] S.R. Bandler et al., "Performance of TES X-ray Microcalorimeters with a novel design", *J.Low Temp. Phys.* 151, pp.400, 2008.
- [4] J.N. Ullom et al., "Optimized transition-edge-sensor x-ray microcalorimeter with 2.4 eV energy resolution at 5.9 KeV" *Appl. Phys. Lett.* 87, 194103 (2005)
- [5] L. Gottardi et al., "Development of TES-based detectors array for the x-ray integral field unit (X-IFU) on the future x-ray observatory Athena" *Proc. SPIE* pp. 9144-93, Space Telescopes and Instrumentation 2014: Ultraviolet to Gamma Ray, 91442M (2014)
- [6] J. N. Ullom and D.A. Bennett, "Review of superconducting TES for X-ray and γ -ray astrophysics" *Supercond. Sci. Technol.* 28, pp. 084003 (2015)
- [7] A.D. Brown et al., "Absorber materials for transition-edge sensor X-ray microcalorimeters", *J. Low Temp. Phys.*, 151, pp. 413, 2008.
- [8] R. González-Arrabal et al., "Mo/Au bilayers deposited by sputtering at room temperature for transition edge sensors fabrication", *J. Low Temp. Phys.* 151, pp. 239, 2008.
- [9] M. Parra-Borderías et al., "Characterization of a Mo/Au thermometer for Athena", *IEEE Trans. Appl. Supercond.* 23, pp. 2300405, 2013.
- [10] L. Fàbrega et al., "Mo-based proximity bilayers for TES: microstructure and properties", *IEEE Trans. Appl. Supercond.* 19, pp 460, 2009.
- [11] L. Fàbrega et al., "Towards Mo/Au based TES detectors for Athena/X-IFU", *Proc. SPIE Conf. Series*, vol. 9144, 91445P, 2014.
- [12] L. Fàbrega et al., "Size and dimensionality effects in superconducting Mo thin films", *Supercond. Sci. Technol.* 24, 075014, 2011.
- [13] G.C.Hilton et al., "Microfabricated Transition-Edge X-ray Detectors", *IEEE Trans. Appl. Supercond.* 11, pp. 739, 2001.
- [14] J.Moral-Vico et al., "Electrodeposition variables modulating the properties of Bi coatings for X-ray absorbers", submitted to *Electrochem. Comm.*
- [15] E. Sandnes, ME Williams, U Bertocci, MD Vaudin, GR Stafford, "Electrodeposition of bismuth from nitric acid electrolyte." *Electrochimica acta* 52, pp. 6221-6228, 2007.
- [16] M. Yang, Z. Hu, "Electrodeposition of bismuth onto glassy carbon electrodes from nitrate solutions", *Journal of electroanalytical chemistry* 583, pp. 46-55, 2006.
- [17] P. M. Vereecken, P. C. Seanson, "Electrochemical formation of GaAs/Bi Schottky barriers.", *Applied physics letters* 75(20) pp. 3135-3138, 1999.
- [18] C. A. Hoffman et al., "Semimetal-to-semiconductor transition in bismuth thin films", *Phys. Rev. B* 48, pp. 11431, 1993.
- [19] D. Drung, C. Amann, J. Beyer, A. Kirste, M. Peters, F. Ruede, "Highly sensitive and esasy-to-use SQUID sensors", *Paper 5EB01 at ASC2006*
- [20] K. Kinnunen "Studies of transition-edge sensor physics: thermal models and noise", *PhD Thesis*.
- [21] I. J. Maasilta and K. Kinnunen, "New Analysis Method for IV and Complex Impedance Data of Transition-Edge Sensors", *AIP Conf. Proc.*, 1185, pp. 38, 2009.
- [22] M. A. Lindeman et al., "Impedance measurements and modeling of a transition-edge sensor calorimeter", *Rev. Sci. Instr.*, 75, pp. 1283, 2004.
- [23] M. A. Lindeman et al., "Complex impedance measurements for calorimeters and bolometers", *Rev. Sci. Instr.*, 78, pp. 043105, 2007.
- [24] E. Taralli et al., "Impedance measurements for photon number resolving Transition-Edge Sensors", *Eur. Phys. J. Plus*, 127, pp. 13, 2012.
- [25] M. A. Lindeman et al., "Relationship Between Complex Impedance, Thermal Response, and Noise in TES Calorimeters and Bolometers", *IEEE Trans. Appl. Supercond.*, vol.21, no. 3, Jun. 2011.
- [26] M. Galeazzi and D. McCammon, "Microcalorimeter and bolometer model", *J. Appl. Phys.*, 93 pp. 4856, 2003.
- [27] M. R. J. Palosaari et al., "Analysis of impedance and noise data of an X-ray transition edge sensor using complex thermal models", *J. Low Temp. Phys.*, 167, pp. 129, 2012.
- [28] I. J. Maasilta, "Complex impedance, responsivity and noise of transition-edge sensors: Analytical solutions of two- and three-block thermal models", *AIP Advances* 2, pp. 042110, 2012.
- [29] Y. Takei et al., "Characterization of high-performance Ti/Au TES microcalorimeter with a central Cu absorber", *J. Low Temp. Phys.* 151, pp 161, 2008.
- [30] Y. Zhao et al., "Study of excess heat capacity and suppressed Kapitza conductance in TES devices", *IEEE Trans. Appl. Supercond.* 21, 227, 2011.

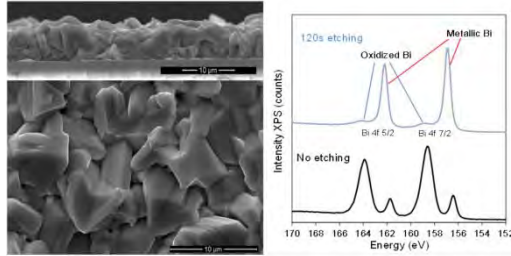


Fig. 1. (left) SEM image of the microstructure and profile of an optimal electrodeposited Bi film. (right) XPS spectra of Bi 4f peaks for an as-deposited film (bottom) and after etching the surface with Ar⁺ ions during 120 s (top). It evidences that most of the Bi oxide disappears after the latter etching, which corresponds to ~20 nm, leaving only pure, metallic Bi.

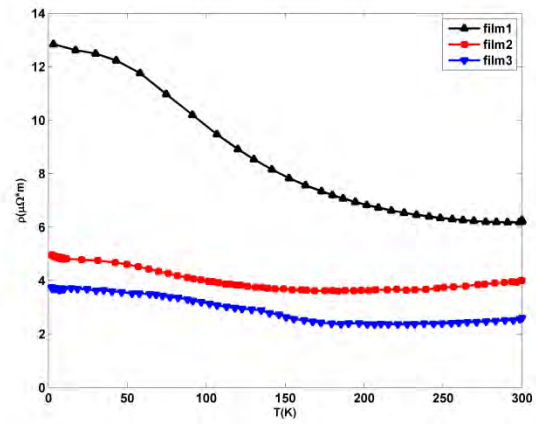


Fig. 2. Temperature dependence of resistivity of three Bi films with ~6 μm thickness: films 2 and 3 were obtained with the optimal electrodeposition conditions found respectively for solutions 1 and 2 described in the text (static process and heating in the first case, dynamic process and heating in the second case). Film 1, synthesized from solution 1 without heating, is representative of films far from optimal. The data were taken using 4-probe measurements and subtracting the measured contribution of the underlying metal film (10 nm Au/2 nm Cr).

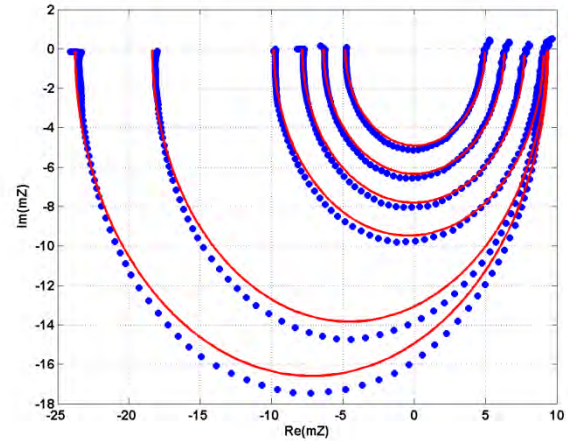


Fig. 3. Z_{TES}(ω) curves (dots) for Device_B at 80 mK and different points along its superconducting transition, from 29% to 73% of R_n. Solid lines are fits to a single block thermal model.

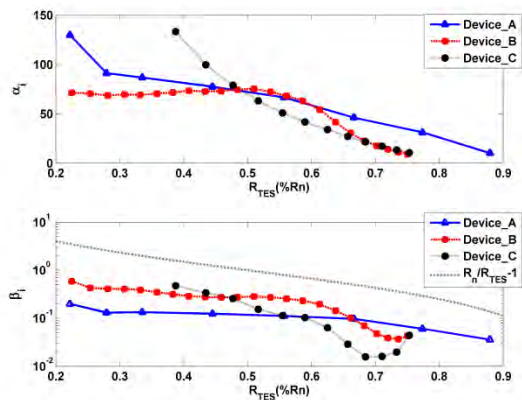


Fig. 4. α₁ (top) and β₁ (bottom) along the superconducting transition for the three TES measured at 80 mK. Dashed-dot line delimits the two-fluid regime [6]

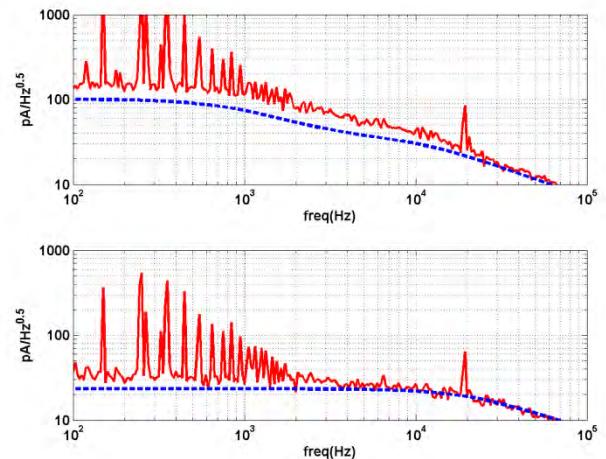


Fig. 5. Noise spectra for Device_B at 80 mK recorded at two points of the transition, 35% R_n and 80% R_n. The solid line is the measured data, while the dashed line is the predicted noise for a simple thermal block, including 3 pA/Hz^{0.5} to account for the SQUID noise.